Supplementary Information

Achieving over 90 % initial Coulombic efficiency and highly stable Li storage in SnO_2 by constructing interfacial oxygen redistribution in multilayers

Xuexia Lan†[a], Jie Cui†[b], Xiaofeng Zhang†[c], Renzong Hu*[a], Liang Tan[a], Jiayi He[a], Houpo Zhang[a], XingYu Xiong[a], Xianfeng Yang[b], Shunqing Wu*[c], and Min Zhu*[a]

[a] School of Materials Science and Engineering, Guangdong Provincial Key Laboratory of Advanced Energy Storage Materials, South China University of Technology, Guangzhou, 510640, China

[b] Analytical and Testing Center, South China University of Technology, Guangzhou, 510640, China

[c] Department of Physics, OSED, Key Laboratory of Low Dimensional Condensed Matter Physics (Department of Education of Fujian Province), Jiujiang Research Institute, Xiamen University, Xiamen, 361005, China

† These authors contributed equally.

* Corresponding Author.

E-mail addresses: msrenzonghu@scut.edu.cn (Renzong Hu)

wsq@xmu.edu.cn (Shunqing Wu)

memzhu@scut.edu.cn (Min Zhu)

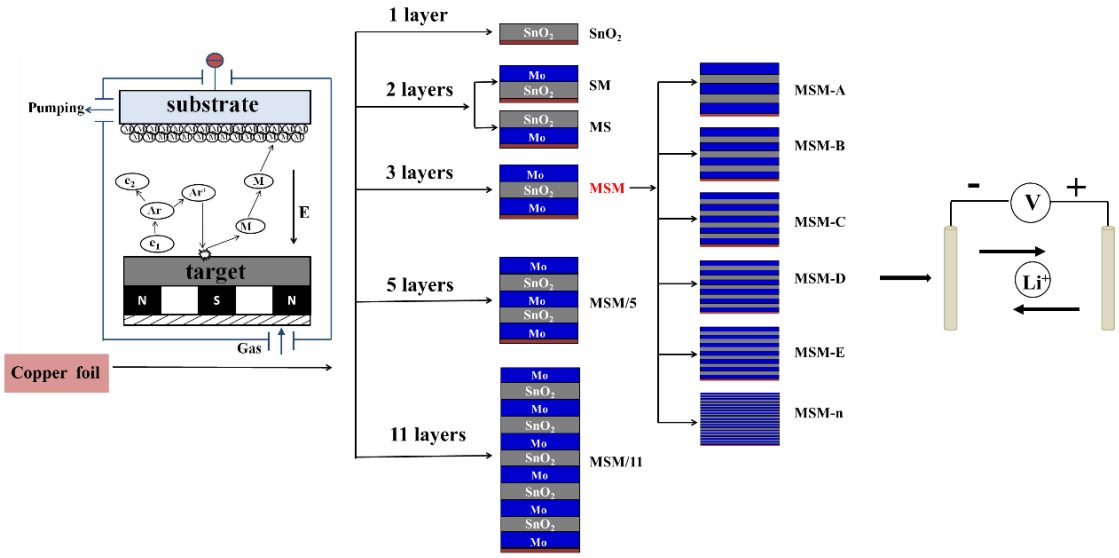

Figure S1. Schematic illustration of the SnO_2-Mo multilayered electrodes preparation procedures. (a) Depositing the SnO_2-Mo multilayers on the copper foil current collector. (b) Assembling Li-ion cells to evaluate the electrochemical performance of the SnO_2-Mo multilayered electrodes.

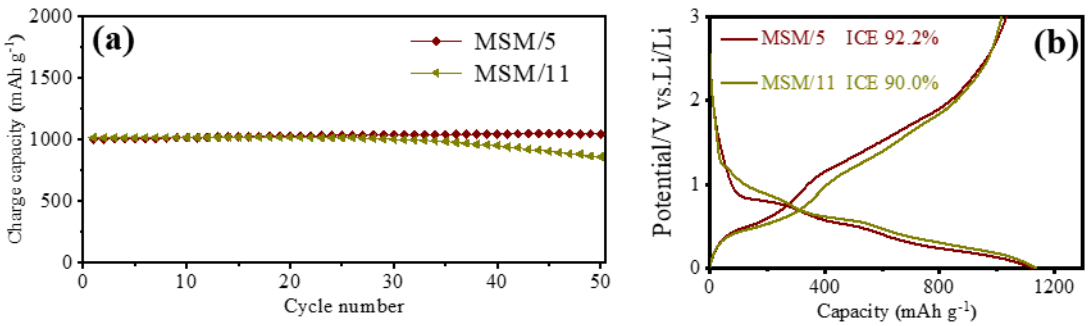

Figure S2. Cycling performance and discharge/charge profiles of the MSM/5 and MSM/11 electrodes.

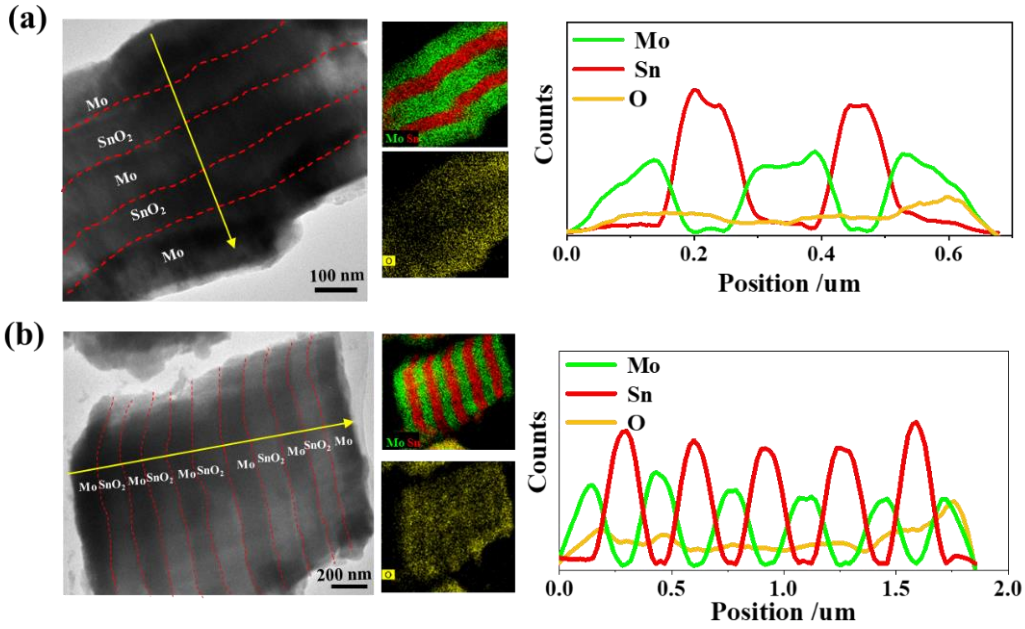

Figure S3. TEM images of cross-sectional morphology and EDS images for MSM/5 (a) and MSM/11 (b) electrodes.

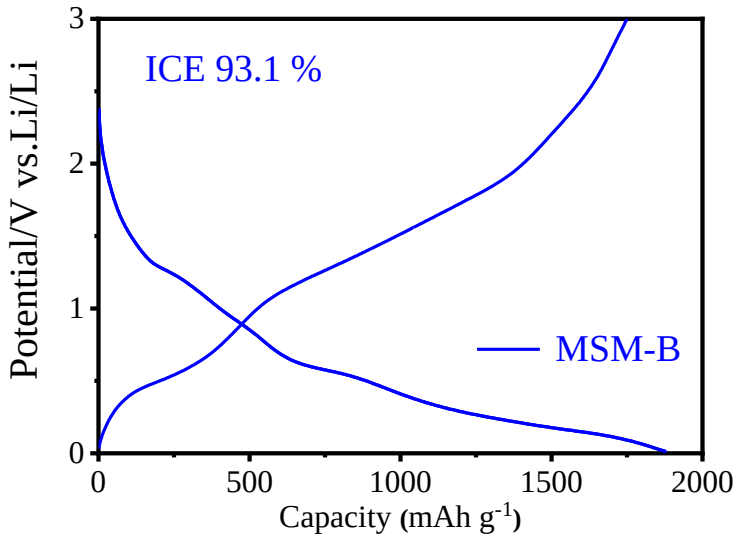

Figure S4. Discharge/charge profiles of the MSM-B electrode.

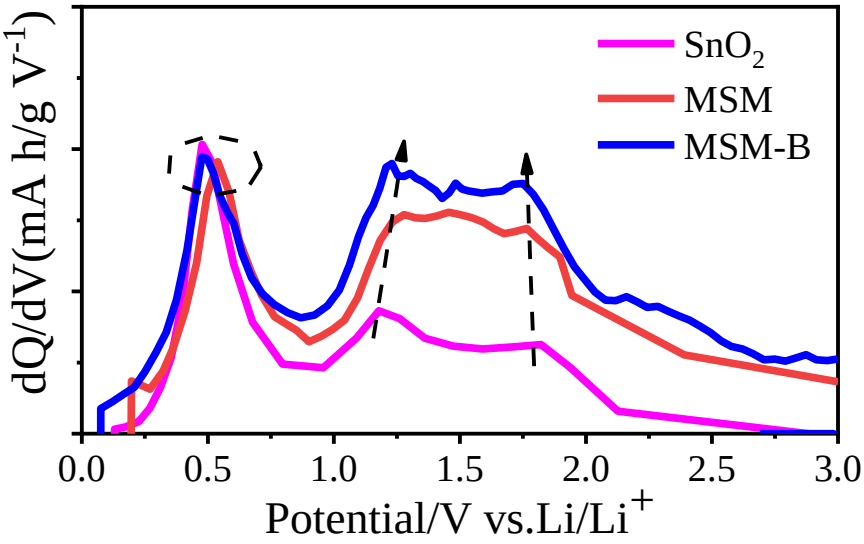

Figure S5. Differential charge capacity vs. voltage curve of the SnO_2, MSM and MSM-B electrodes at the 1st cycle.

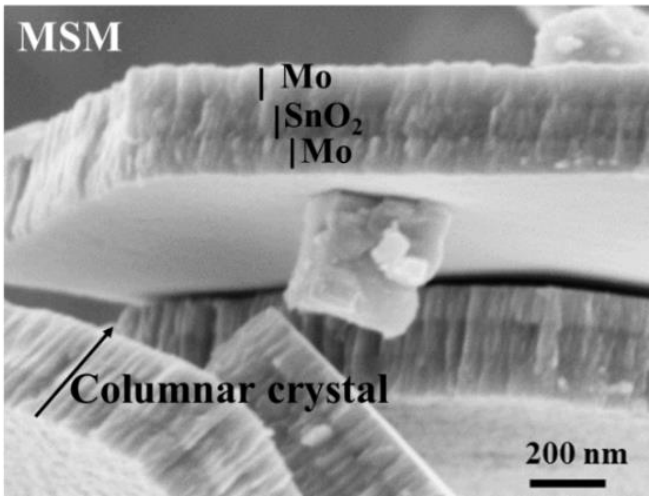

Figure S6. SEM image of cross-sectional morphology for the MSM electrode.

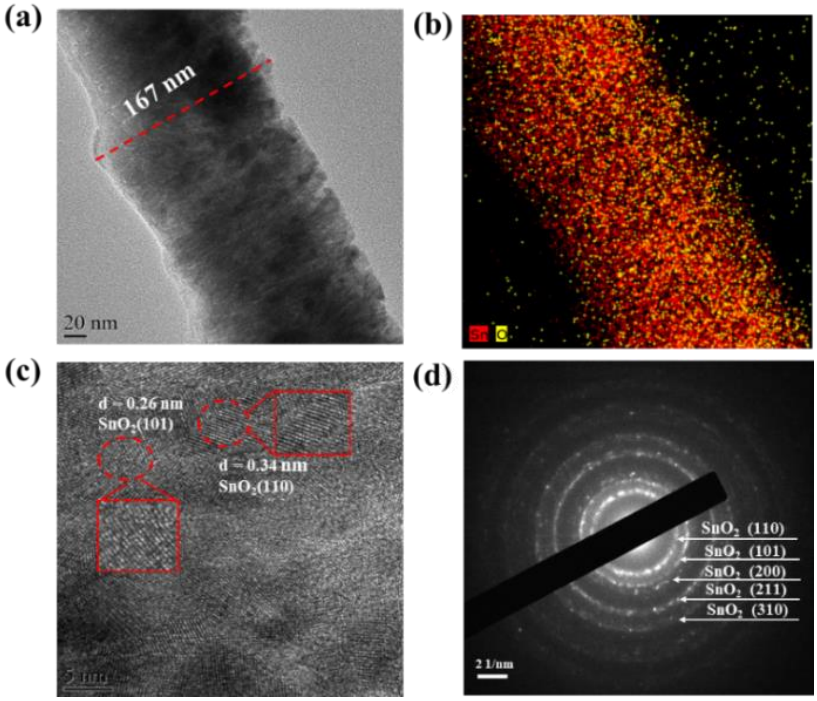

Figure S7. TEM images of cross-sectional morphology and phase observation for the SnO_2 electrode. (a) Typical TEM image of cross-sectional morphology. (b) EDS mapping images with Sn and O elements. (c) HRTEM image. (d) SAED image.

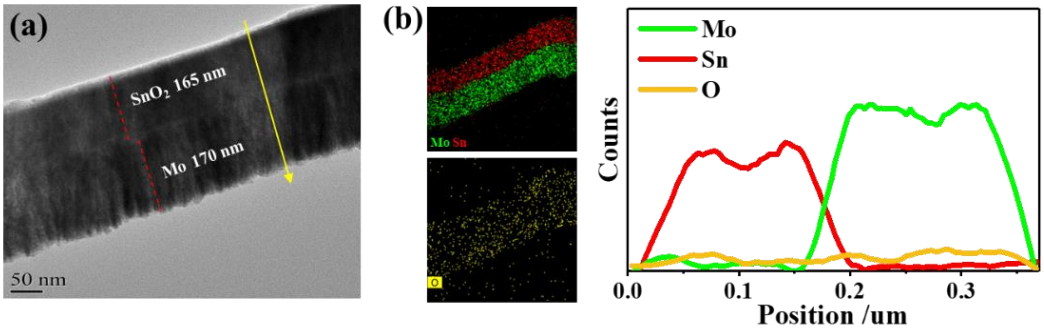

Figure S8. TEM image of cross-sectional morphology (a) and EDS images (b) for SM electrode.

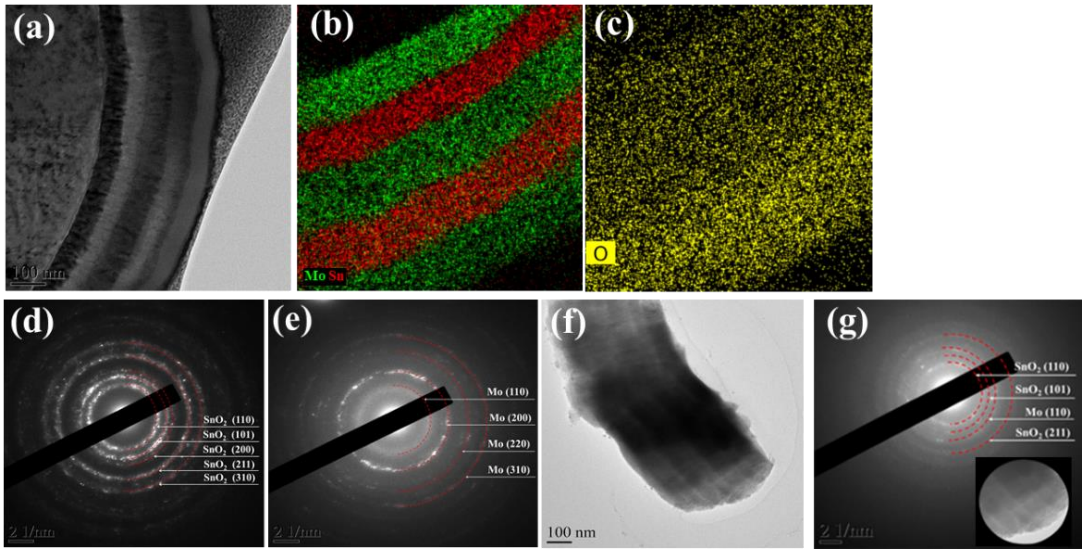

Figure S9. TEM images of cross-sectional morphology and phase observation for MSM-A (a-e) and MSM-B (f, g) electrodes. (a) Typical TEM image of cross-sectional morphology. (b, c) EDS mapping of Sn, Mo and O elements. (d) SAED image of SnO_2 layer. (e) SAED image of Mo layer. (f) TEM cross-sectional morphology image. (g) SAED image (insert image shows the selected part).

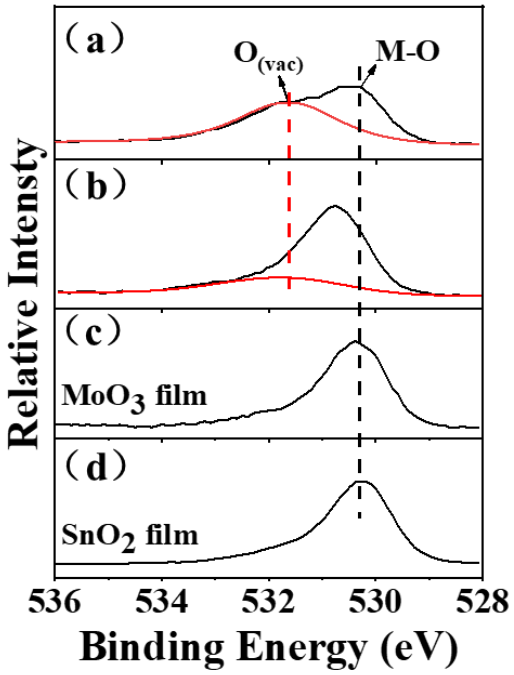

Figure S10. XPS spectra of O 1s. (a) at the up side of interface in MSM. (b) at the

down side of interface in MSM. (c) SnO_2 films. (d)MoO_3 films.

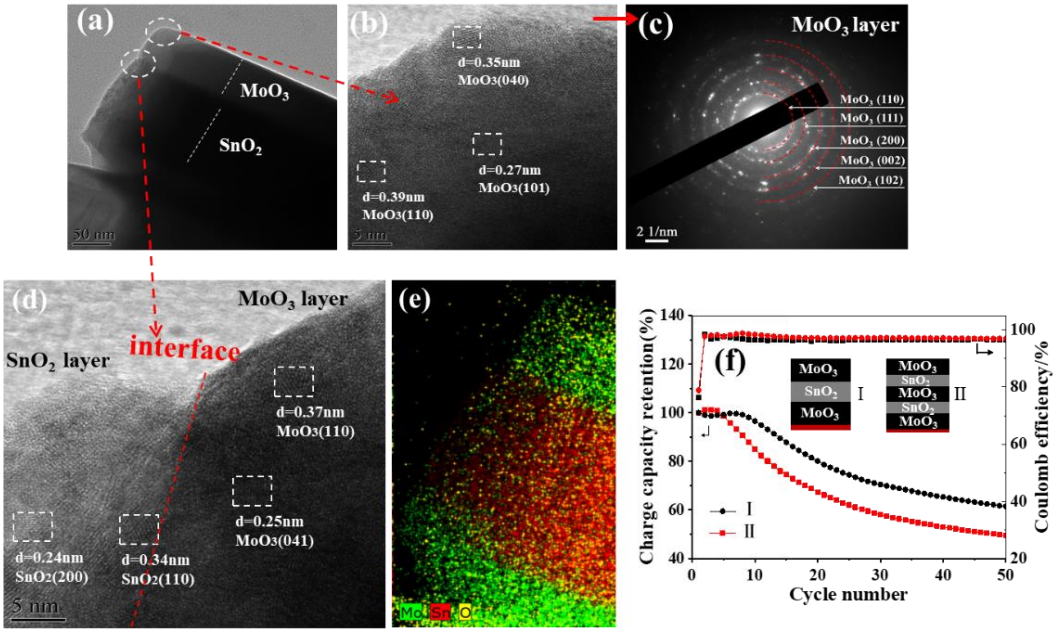

Figure S11. (a-e) TEM observation for the $MoO_3/SnO_2/MoO_3$ electrode. (a) Typical cross-sectional morphology. (b) HRTEM image of the MoO_3 layer. (c) SAED image of the MoO_3 layer. (d) HRTEM image at the interface between MoO_3 and SnO_2 layers. (e) EDS mapping image of Sn, Mo and O elements. (f) Cycling performance of MoO_3-SnO_2 electrodes.

The HRTEM and SAED images for MoO_3 layer demonstrate the polycrystalline state of MoO_3 (Figure S11b, c). From the locally magnified HRTEM image at the interface between MoO_3 and SnO_2 layer (Figure S11d), obvious lattice fringes for MoO_3 and SnO_2 can be observed, indicating high crystallinity, which is significantly different from the amorphous interfaces in the MSM. Figure S11f displays the cycling performance of $MoO_3/SnO_2/MoO_3$ and $MoO_3/SnO_2/MoO_3/SnO_2/MoO_3$ electrodes. After 50 cycles, the $MoO_3/SnO_2/MoO_3$ achieves a charge capacity retention of 61.4 %, much lower than that of the MSM. Furthermore, the charge capacity retention further

decreased to 49.5 % for the $MoO_3/SnO_2/MoO_3/SnO_2/MoO_3$ with greater interfacial density, showing the negative effects of the interface in the MoO_3-SnO_2 electrodes.

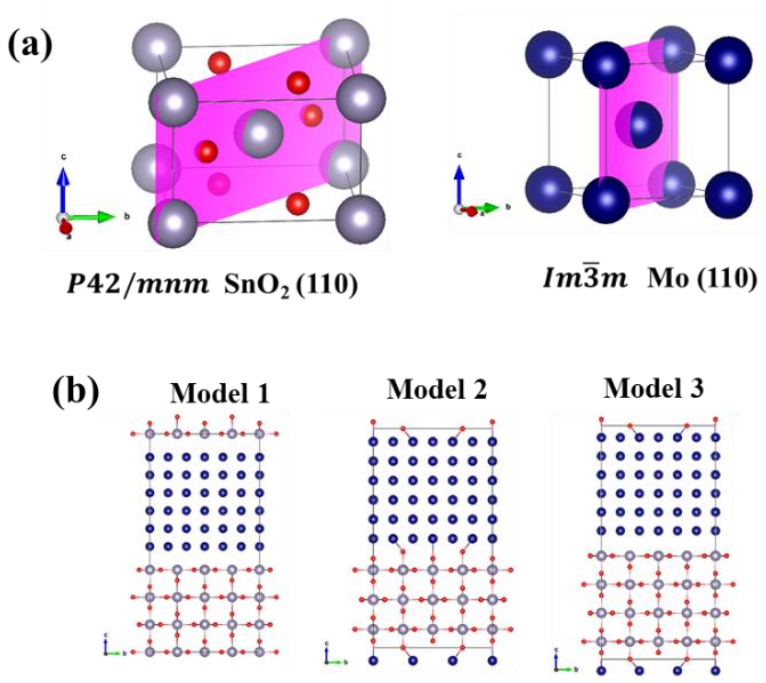

Figure S12. (a) Crystal structures of SnO_2 and Mo viewed along the [001] direction. (b) Three SnO_2/Mo interface models.

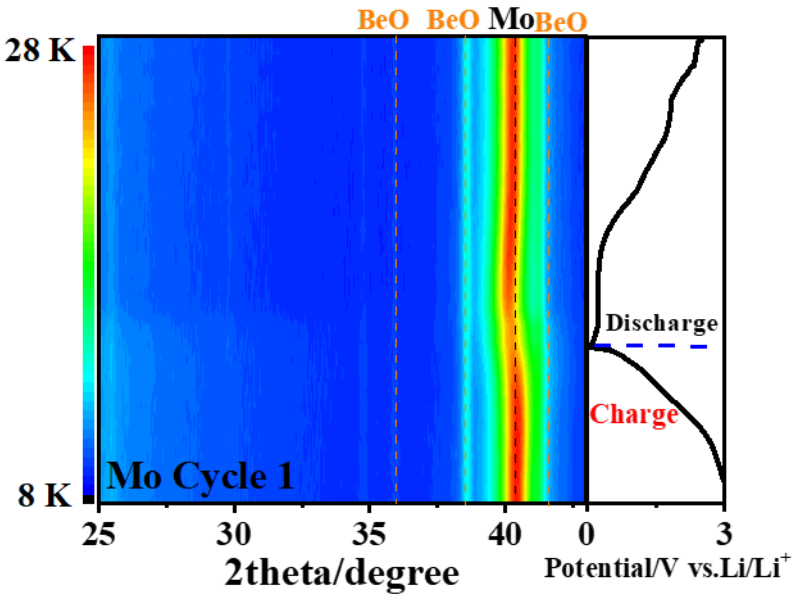

Figure S13. In-situ XRD phase evolution of Mo during lithiation/delithiation

processes.

For the pure Mo film shown in Figure S13, no additional phases or impurities are presented throughout the initial cycle due to the inactivity of Mo to Li^+. However, the diffraction peak of Mo slightly weakens and shifts to the lower 2θ values when discharging to low potential, while increases and shifts to the higher 2θ values again when charging. The variation of the Mo diffraction peak reflects the existence of interaction between Mo layers and the electrolyte due to that Mo allows the solid electrolyte interface (SEI) to form directly on its surface.[1]

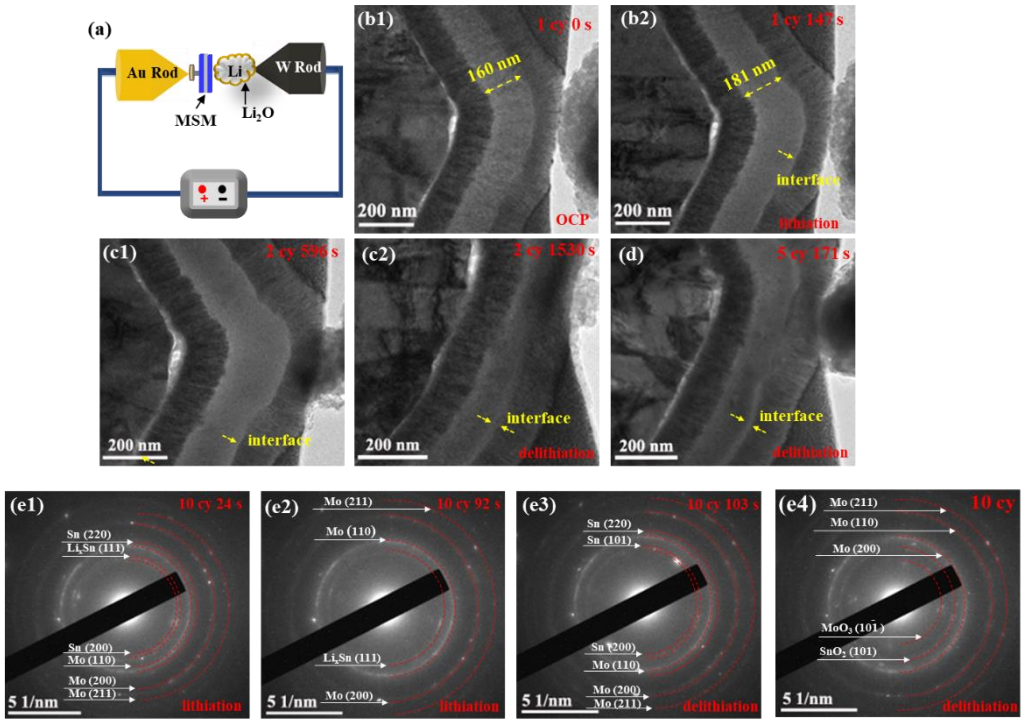

Figure S14. In-situ TEM observation of morphology and phase evolution of MSM electrode during lithiation/delithiation process. (a) Schematic illustration of in situ TEM measurement. (b-d) Sequential images of Li^+ insertion/extraction in the 1st cycle (b), 2nd cycle (c), 5th cycle (d). (e) In situ SAED images operated at various states during the 10th cycle.

As illustrated in Figure S14a, the metallic Li@Li_2O and the MSM film are fixed on the W and Au tips, acting as the counter electrode and working electrode, respectively. During the 1st lithiation process, slight thickness increase about 13 % of SnO_2 layer is observed (Figure S14b1, b2), indicating the occurrence of rapid Li^+ insertion (Video S1). Compared with the previous reported results of fully lithiated SnO_2 with 370 % volume expansion,[2, 3] the minor volume variation confirms that the volume effect can be effectively prevented in the MSM. After the 1st full delithiation (Figure 6f), the thickness of SnO_2 layer demonstrates a volume shrinkage. Furthermore, during the following several rapid lithiation/delithiation processes (Figure S14c, d and Figure 6g), the MSM remains high structure integrity guaranteed by the protection of Mo layers and the coordination effect of the amorphous interfaces composed of mixed metal oxides with stabilization effect,[4] which is completely different from the pure SnO_2 electrode (Video S2)

The interfical effect on the reversibility of electrochemical reactions was also investigated through the in-situ SAED patterns during the 10th cycle, and the demonstrated phase evolution is consistent with the in-situ XRD results. Figure S14e and Video S1 display the in-situ SAED patterns during the 10th cycle. In the early process of lithiation (Figure S14e1), the diffraction pattern is mainly composed of Mo, Sn, accompanied by a small amount of Li_xSn, corresponding to the conversion reaction of SnO_2. Then, the disappearance of Sn and the increase of Li_xSn reveal the occurrence of an alloying reaction (Figure S14e2). In the delithiation process, the dealloying

reaction first happens with the diffraction rings of Sn (Figure S14e3), In the fully delithiated status (Figure S14e4), the disappearance of Sn phase again indicates the completion of reversed conversion reaction. Furthermore, the emergence of metal oxides (SnO_2, MoO_3) demonstrates superior reaction reversibility as the cycle proceeds.[5] These also clearly confirm that SnO_2 is the dominant reactant in these SnO_2-Mo multilayers.

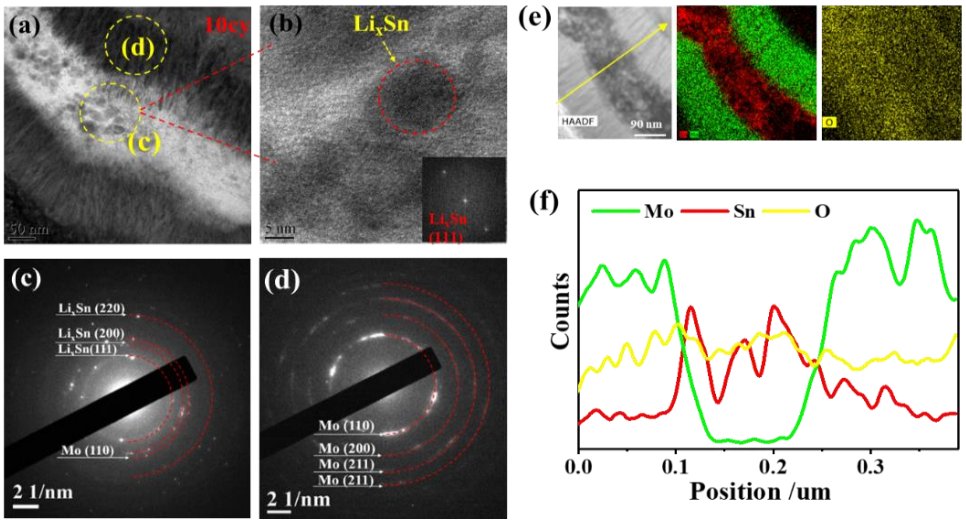

Figure S15. In-situ TEM observation of morphology and phase evolution of MSM electrode at the fully lithiated status in the 10th cycle. (a) Typical cross-sectional morphology. (b) HRTEM image of the SnO_2 layer. (c, d) SAED images of the SnO_2 and Mo layers as marked in (a). (e, f) HADDF image, EDS mapping and line-scan images.

Figure S15 shows in-situ TEM observation for the MSM electrode at the fully lithiated state after 10 cycles. Obviously, the Li_xSn particles with a size of 5-10 nm have been generated (Figures S15a-d). More apparent interdiffusion between SnO_2 and Mo layers happens as the cycles increase, and O tends to concentrate at the interfaces

(Figure S15e, f). As a result, the interfaces tend to capture more Li^+ during discharge and contribute more additional capacity to the multilayers electrodes. More importantly, the concentration of O at the SnO_2/Mo interfaces would induce an increase of oxygen vacancy in the SnO_2 layer, which promotes the reversibility of conversion reactions in lithiated SnO_2.[2]

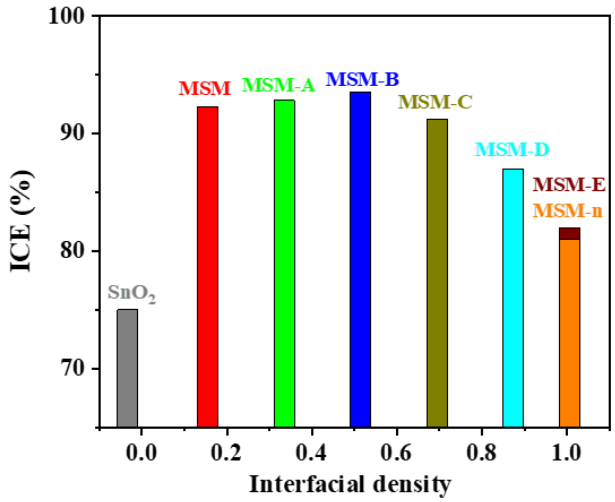

Figure S16. Comparison of the ICEs for SnO_2, MSM, MSM-A, MSM-B, MSM-C, MSM-D, MSM-E and MSM-n electrodes.

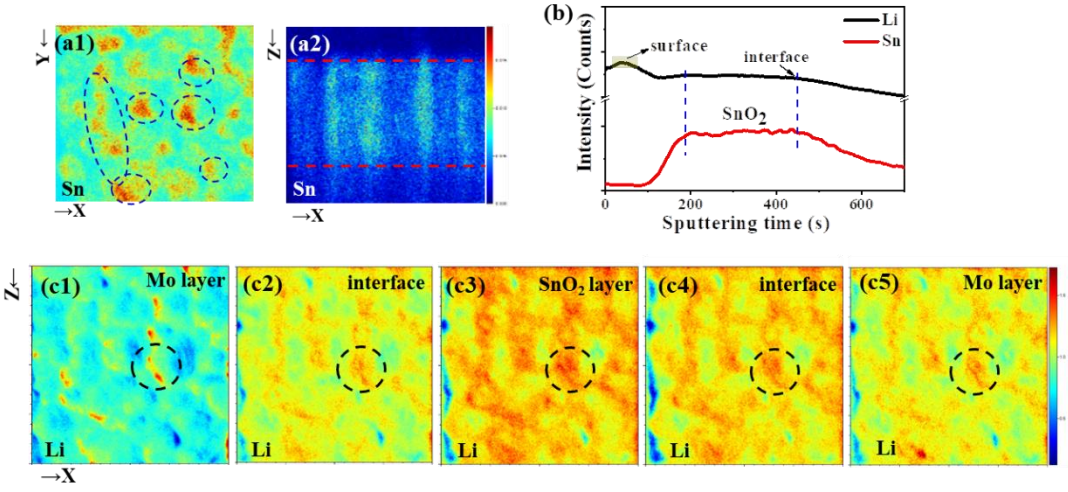

Figure S17. TOF-SIMS for MSM electrode as discharged to 0.01V in 1st cycle after the scavenging process, showing the distribution of Li. (a) Li distributed along the XY plane (a1) and XZ plane (a2). (b) Depth profiles of Li. (c) Distribution of Li with increasing depth along the XY plane. The depth positions are taken from (b).

In the fully lithiated state (discharged to 0.01V), after a scavenging process, as displayed in Figure S17a, b, Sn is mainly distributed in the middle layer and slightly diffuses to the Mo layers. The content of Li in MSM electrode as discharged to 0.01V in 1st cycle, as displayed in Figure S17b, c, in SnO_2 layer is the highest, followed by the interfaces, and the Mo layer is the lowest. It should be mentioned that the exceptionally high Li content on the surface results from the SEI and is not discussed further.

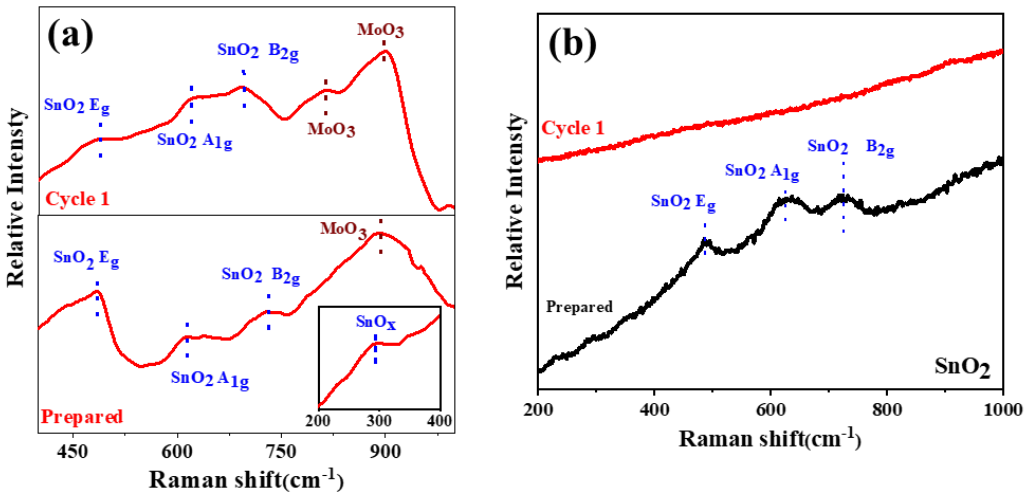

Figure S18. SERS spectra of SnO_2 electrode before and after the 1st cycle.

As displayed in Figure S18a, the pristine MSM shows three obvious bands for the SnO_2 phase at Raman shift around 480, 630, 720 cm^{-1}, corresponding to the E_g

(translational), A_{1g} (symmetric Sn-O stretching), and B_{2g} (asymmetric Sn-O stretching) vibration mode, respectively.[6, 7] Besides, the SnO_x peak at 290 cm^{-1} and MoO_3 peak at 890 cm^{-1} are observed, which come from the interfaces between SnO_2 and Mo layer. The SERS recorded at the end of first charge presents the same peaks of SnO_2, providing the strongest evidence to support that the conversion between Li_2O and SnO_2 is reversible during the discharge/charge cycle of MSM. In contrast, no vibration of SnO_2 can be detected in the pure SnO_2 electrode after the initial cycle (Figure S18b).

Table S1. Preparation conditions and parameters of the various SnO_2-Mo multilayers.

Film		Time (min)	Power	Pressur
SnO_2	SnO_2	3		
Mo/SnO_2	MS	3/3		
SnO_2/Mo	SM	3/3		
Mo/SnO_2/Mo	MSM	3/3/3		
Mo/SnO_2/Mo/SnO_2/Mo (5 layers)	MSM-A	2/1.5/2/1.5/2		
Mo/SnO_2/Mo/SnO_2/Mo/SnO_2/Mo (7 layers)	MSM-B	1.5/1/1.5/1/1.5/1/1.5	120 W	2 Pa
Mo/SnO_2/Mo/SnO_2/Mo/SnO_2/Mo/SnO_2/Mo (9 layers)	MSM-C	1.2/0.75/1.2/0.75/1.2/0.75/1.2/0.75/1.2		
Mo/SnO_2/Mo/SnO_2/Mo/SnO_2/Mo/SnO_2/Mo/SnO_2/Mo (11 layers)	MSM-D	1/0.6/1/0.6/1/0.6/1/0.6/1/0.6/1		
Mo/SnO_2/Mo/SnO_2/Mo/SnO_2/Mo/SnO_2/Mo/SnO_2/Mo/SnO_2/Mo (13 layers)	MSM-E	0.86/0.5/0.86/0.5/0.86/0.5/0.86/0.5/0.86/0.5/0.86/0.5/0.86/0.5		
Mo/SnO_2 /……../SnO_2/Mo (n layers)	MSM-n	Semi-cosputtering		

$Mo/SnO_2/Mo/SnO_2/Mo$ (5 layers)	MSM/5	3/3/3/3/3/3/3/3/3
$Mo/SnO_2/Mo/SnO_2/Mo/SnO_2/Mo/SnO_2/Mo/SnO_2/Mo$ (11 layers)	MSM/11	3/3/3/3/3/3/3/3/3/3/3

1

2

Table S2. Preparation conditions and parameters of the SnO_2-MoO_3 film electrodes

Film		Time	Power	Pressure
$MoO_3/SnO_2/MoO_3$	I	12/3/12 min	120W	2 pa
$MoO_3/SnO_2/MoO_3/SnO_2/MoO_3$	II	8/1.5/8/1.5/8 min		

$$\gamma_{Sn_xO_y/Mo} = \frac{E_{Sn_xO_2/Mo} - E_{Sn_xO_y} - E_{Mo}}{2A}$$

Table S3. Interfacial formation energy of the three SnO_2/Mo interface models.

Model	$\Gamma_{SnxOy/Mo}$ (eV/Å^2)
1	-0.078
2	-0.367
3	-0.209

Table S4. Atomic valence and valence charge for the elements of Mo and Sn at the interface of MSM electrode.

	Mo	Mo^{1+}	Mo^{4+}	Mo^{6+}
Bader charge (e)	6.00	5.46	4.10	3.64
	Sn	Sn^{2+}	Sn^{4+}	
Bader charge (e)	4.00	2.80	1.69	

References

1. Son, S. B. et al. An artificial interphase enables reversible magnesium chemistry in carbonate electrolytes. *Nat. Chem.* **10,** 532-539 (2018).

2. Hu, R. et al. Inhibiting grain coarsening and inducing oxygen vacancies: the roles of Mn in achieving a highly reversible conversion reaction and a long life SnO_2-Mn-graphite ternary anode. *Energy Environ. Sci.* **10,** 2017-2029 (2017).

3. Wang, C. S., Appleby, A. J. & Little, F. E. Electrochemical study on nano-Sn, $Li_{4.4}Sn$ and $AlSi_{0.1}$ powders used as secondary lithium battery anodes. *J. Power Sources*. **93,** 174-185 (2001).

4. Sarkar, A. et al. High entropy oxides for reversible energy storage. *Nat. Commun.* **9,** 3400 (2018).

5. Hu, R. et al. Dramatically enhanced reversibility of Li_2O in SnO_2-based electrodes: the effect of nanostructure on high initial reversible capacity. *Energy Environ. Sci.* **9,** 595-603 (2016).

6. Ma, H. C. et al. Synthesis of visible-light responsive Sn-SnO_2/C photocatalyst by simple carbothermal reduction. *Energy Environ. Sci.* **4,** 3067-3074 (2011).

7. Meduri, P., Clark, E., Dayalan, E., Sumanasekera, G. U. & Sunkara, M. K. Kinetically limited de-lithiation behavior of nanoscale tin-covered tin oxide nanowires. *Energy Environ. Sci.* **4,** 1695-1699 (2011).